# Testing $WW\gamma$ vertex in radiative muon decay

Anirban Karan* and Rahul Sinha†
*The Institute of Mathematical Sciences, Taramani, Chennai 600113, India and Homi Bhabha National Institute, BARC Training School Complex, Anushaktinagar, Mumbai 400094, India*

Rusa Mandal‡
*IFIC, Universitat de València-CSIC, Apartat de Correus 22085, E-46071 València, Spain*

(Received 30 October 2018; published 12 February 2019)

Large numbers of muons will be produced at facilities developed to probe the lepton-flavor-violating process $\mu \to e\gamma$. We show that by constructing a suitable asymmetry, radiative muon decay $\mu \to e\gamma\nu_\mu\bar{\nu}_e$ can also be used to test the $WW\gamma$ vertex at such facilities. The process has two missing neutrinos in the final state, and upon integrating their momenta the partial differential decay rate shows no radiation-amplitude zero. However, we establish that an easily separable part of the normalized differential decay rate that is odd under the exchange of photon and electron energies does have a zero in the case of the standard model (SM). This *new type of zero* has hitherto not been studied in the literature. A suitably constructed asymmetry using this fact enables a sensitive probe for the $WW\gamma$ vertex beyond the SM. With a simplistic analysis, we find that the $C$- and $P$-conserving dimension-four $WW\gamma$ vertex can be probed at $\mathcal{O}(10^{-2})$ with a satisfactory significance level.

DOI: 10.1103/PhysRevD.99.033006

## I. INTRODUCTION

The $SU(2)_L \otimes U(1)_Y$ theory of electroweak interactions has been tested extensively in last few decades and there is no doubt that it is the correct theory at least up to the TeV scale. This conviction is largely based on the precision measurements at LEP and the consistency of the top and Higgs boson masses which could be predicted by taking radiative corrections into account. The gauge boson and Higgs boson self-interactions are, however, not as well probed either by direct measurements or by radiative corrections and it is possible that some deviations from the standard model (SM) loop-level values might still be seen. To ascertain the validity of the SM it is critical that the $WW\gamma$ vertex, which is predicted uniquely in the SM, be probed to an accuracy consistent with loop-level corrections to it. Several experiments [1–8] have measured parameters that probe the $WW\gamma$ and $WWZ$ vertices, but the accuracy achieved is still insufficient to probe one-loop corrections to it within the SM.

*kanirban@imsc.res.in
†sinha@imsc.res.in
‡Rusa.Mandal@ific.uv.es



In this paper, we investigate how the $C$- and $P$-conserving dimension-four $WW\gamma$ operator can be probed experimentally using radiative muon decays. The vertex factor for this operator is usually denoted by $\kappa_\gamma$ and is uniquely predicted in the SM. At tree level, $\kappa_\gamma = 1$ in the SM and the absolute value of the one-loop corrections to the tree-level values of $\kappa_\gamma$ is restricted to be less than $1.5 \times 10^{-2}$ [9]. However, the current global average $\kappa_\gamma = 0.982 \pm 0.042$ [10] has too large an uncertainty to probe the SM up to one-loop accuracy. Of the experimentally measured values of $\kappa_\gamma$, only the ATLAS and CMS collaborations use the data for real on-shell photon emission in hadron colliders [1,2], probing the true magnetic moment of the $W$ boson.

One can expect $\kappa_\gamma$ to deviate from its SM value by only a few percent; hence, we must choose the mode to be studied very carefully. Radiative muon decay $\mu \to e\gamma\nu_\mu\bar{\nu}_e$ is a promising mode to measure the true magnetic moment (due to a real photon in the final state) of the $W$ boson in this regard. At first sight the measurement of the $W$-boson gauge coupling using a low-energy decay process may seem impossible, since the effect is suppressed by two powers of the $W$-boson mass. The process has two missing neutrinos in the final state, and upon integrating their momenta the partial differential decay rate shows no radiation-amplitude zero [11]. Moreover, the differential decay rate does not show enough sensitivity to a deviation of the $WW\gamma$ vertex from that of the SM. We show, however, that an easily separable part of the normalized differential decay rate (odd under the exchange of photon and electron energies) does have a zero in the case of the SM. The vanishing of the odd contribution under the exchange of the final-state electron and photon energies in the decay rate is a *new type of zero* that hitherto has not been studied in the literature. A suitably constructed asymmetry using this fact enables adequate sensitivity to probe the $WW\gamma$ vertex beyond the SM. We consider a very restricted part of the phase space where the asymmetry is larger than statistical errors for our study. A large number of muons are expected to be produced at the COMET [12], MEG [13], and Mu2e [14] experiments to probe lepton-flavor-violating processes like $\mu \to e\gamma$. The radiative muon decay $\mu \to e\gamma\nu_\mu\bar{\nu}_e$ [15] discussed in this paper is the dominant background process for this case. The large sample of $\mu \to e\gamma\nu_\mu\bar{\nu}_e$ produced at such facilities makes them an ideal environment to probe the $WW\gamma$ vertex, with reduced statistical uncertainty, as discussed in this paper. In a simulation using $\eta_\gamma \equiv \kappa_\gamma - 1 = 0.01$, we find that the asymmetry constructed by us can probe this $\eta_\gamma$ value with $3.9\sigma$ significance.

The rest of the paper is organized as follows. In Sec. II we briefly discuss the decay kinematics and relevant expressions for the decay rate. These results are used to construct the observables in Sec. III, where we also explain why a zero in the odd amplitude is expected. Section IV deals with the numerical analysis to probe the $WW\gamma$ vertex, and finally we conclude in Sec. V.

## II. THEORETICAL FRAMEWORK

In this section we briefly discuss the theoretical setup for the radiative muon decay. The radiative muon decay proceeds through three Feynman diagrams, shown in Fig. 1, where the photon in the final state can either arise from any of the initial- and final-state leptons or the $W$ boson in the propagator. The latter process is what we are interested in. We define the four-momenta of an incoming $\mu^-$, outgoing $e^-$, $\gamma$, $\nu_\mu$, and $\bar{\nu}_e$ as $p_m$, $p_e$, $p$, $k$, and $k'$, respectively, and the masses of the muon, electron, and $W$ boson are denoted by $m_\mu$, $m_e$, and $m_W$, respectively. The amplitudes corresponding to these three diagrams (from top to bottom), labeled with subscripts 1 to 3, can be expressed as

$$i\mathcal{M}_1 = \left(\frac{-ieg^2}{8}\right)\bar{u}(p_e)\gamma_\beta(1-\gamma_5)v(k')\left[\frac{g^{\alpha\beta} - \frac{q_1^\alpha q_1^\beta}{m_W^2}}{q_1^2 - m_W^2}\right] \times \bar{u}(k)\gamma_\alpha(1-\gamma_5)\left[\frac{1}{\not{p}_m - \not{p} - m_\mu}\right]\gamma_\delta u(p_m)\epsilon^{*\delta}, \quad (1)$$

$$i\mathcal{M}_2 = \left(\frac{-ieg^2}{8}\right)\bar{u}(k)\gamma_\alpha(1-\gamma_5)u(p_m)\left[\frac{g^{\alpha\beta} - \frac{q_2^\alpha q_2^\beta}{m_W^2}}{q_2^2 - m_W^2}\right] \times \bar{u}(p_e)\gamma_\delta\left[\frac{1}{\not{p}_e + \not{p} - m_e}\right]\gamma_\beta(1-\gamma_5)v(k')\epsilon^{*\delta}, \quad (2)$$

$$i\mathcal{M}_3 = \left(\frac{-ieg^2}{8}\right)\bar{u}(k)\gamma_\alpha(1-\gamma_5)u(p_m)\left[\frac{g^{\alpha\rho} - \frac{q_2^\alpha q_2^\rho}{m_W^2}}{q_2^2 - m_W^2}\right] \times \left[\frac{g^{\sigma\beta} - \frac{q_1^\sigma q_1^\beta}{m_W^2}}{q_1^2 - m_W^2}\right]\bar{u}(p_e)\gamma_\beta(1-\gamma_5)v(k') \times \Gamma_{\rho\sigma\delta}(q_2, q_1, p)\epsilon^{*\delta}, \quad (3)$$

where $e$ and $g$ are the charge of the positron and the weak coupling constant, respectively, $q_1^\mu = p_e^\mu + k'^\mu$, and $q_2^\mu = p_m^\mu - k^\mu$. In Eq. (3), $\Gamma_{\rho\sigma\delta}(q_2, q_1, p)$ denotes the effective triple gauge boson vertex for electroweak interactions, as shown in Fig. 2.

The most general couplings of $W$ to the neutral gauge bosons $\gamma$ and $Z$ can be described by the following effective Lagrangian [16]:

$$\mathcal{L}_{\text{eff}}^V = -ig_V\Big[g_1^V(W_{\mu\nu}^\dagger W^\mu - W^{\dagger\mu}W_{\mu\nu})V^\nu + \kappa_V W_\mu^\dagger W_\nu V^{\mu\nu} + \frac{\lambda_V}{m_W^2}W_{\lambda\mu}^\dagger W_\nu^\mu V^{\nu\lambda} + if_4^V W_\mu^\dagger W_\nu(\partial^\mu V^\nu + \partial^\nu V^\mu) - if_5^V\epsilon^{\mu\nu\rho\sigma}(W_\mu^\dagger \overleftrightarrow{\partial}_\rho W_\nu)V_\sigma + \tilde{\kappa}_V W_\mu^\dagger W_\nu \tilde{V}^{\mu\nu} + \frac{\tilde{\lambda}_V}{m_W^2}W_{\lambda\mu}^\dagger W_\nu^\mu \tilde{V}^{\nu\lambda}\Big]. \quad (4)$$

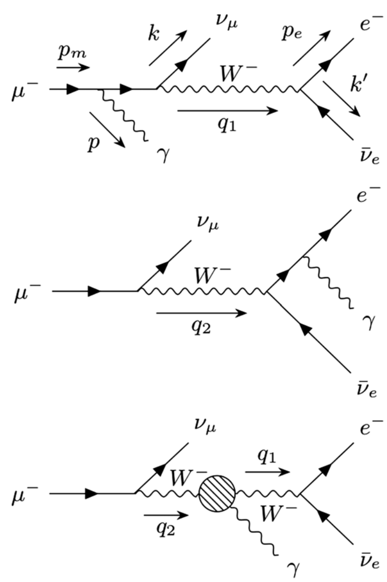


FIG. 1. Feynman diagrams for radiative muon decay.

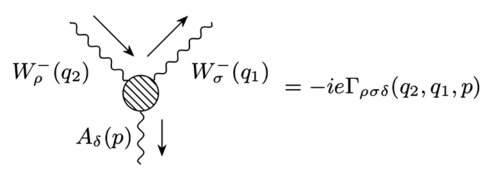


FIG. 2. Feynman rule for the effective $WW\gamma$ vertex.

Here, $V$ corresponds to $\gamma$ or $Z$, $g_\gamma = e$, and $g_Z = e\cot\theta_W$, where $\theta_W$ is the Weinberg angle. $W_{\mu\nu} = \partial_\mu W_\nu - \partial_\nu W_\mu$, $V_{\mu\nu} = \partial_\mu V_\nu - \partial_\nu V_\mu$, $\tilde{V}_{\mu\nu} = \frac{1}{2}\epsilon_{\mu\nu\rho\sigma}V^{\rho\sigma}$, $(A\overleftrightarrow{\partial}_\mu B) = A(\partial_\mu B) - (\partial_\mu A)B$, and the Bjorken-Drell metric is taken as $\epsilon_{0123} = -\epsilon^{0123} = +1$. In the SM, at tree level, $g_1^V = \kappa_V = 1$ and all other coupling parameters are zero.

In the case of radiative muon decay, the vertex with a $W$-boson pair and a photon field is involved, where among the seven coupling parameters, $f_4^\gamma$, $\tilde{\kappa}_\gamma$, and $\tilde{\lambda}_\gamma$ denote the coupling strengths of $CP$-violating interactions in the Lagrangian [in Eq. (4)] and are constrained to be less than $\sim(10^{-4})$ [17] due to the measurements of the neutron electric dipole moment in the case of direct $CP$ violation. Due to the $CP$-violating nature of these couplings, deviations from the SM contributions are proportional to the square of these couplings and thus are highly suppressed, as compared to $CP$-conserving contributions. Hence, we neglect the $CP$-violating parameters for the rest of the paper. The demand that $C$ and $P$ be conserved separately in the Lagrangian allows us to choose a vanishing $f_5^\gamma$. It is obvious that the muon radiative decay will not be sensitive to the dimension six-operator involving $\lambda_\gamma$, due to an additional $m_W^2$ suppression. The measurement of $\lambda_\gamma$ is possible only at high-energy colliders. Hence, we can safely neglect the deviation of $\lambda_\gamma$ from its SM value of zero. Furthermore, the value of the coupling $g_1^\gamma$ is fixed to be unity due to electromagnetic gauge invariance. Thus, in momentum space the $WW\gamma$ vertex can be expressed as

$$\Gamma_{\rho\sigma\delta}(q_2, q_1, p) = g_{\rho\sigma}(q_2 + q_1)_\delta + g_{\sigma\delta}(p - q_1)_\rho - g_{\delta\rho}(p + q_2)_\sigma + \eta_\gamma(p_\rho g_{\sigma\delta} - p_\sigma g_{\rho\delta}), \tag{5}$$

where $\eta_\gamma \equiv \kappa_\gamma - 1$ and $q_2$, $q_1$, and $p$ are the four-momenta of the incoming $W^-$, outgoing $W^-$, and outgoing photon, respectively, as depicted in Fig. 2.

It is apparent from Fig. 1 and Eqs. (1)–(3) that the amplitude $\mathcal{M}_3$ containing the effective vertex $\Gamma_{\rho\sigma\delta}$ is $1/m_W^2$ suppressed compared to the other two contributions $\mathcal{M}_1$ and $\mathcal{M}_2$. Hence, within the SM, the first two Feynman diagrams in Fig. 1 are sufficient to study the process. On the other hand, only the third diagram is sensitive to $\eta_\gamma$. Thus, in order to retain sensitivity to $\eta_\gamma$ in $\Gamma_{\rho\sigma\delta}$, it is necessary and sufficient to keep contributions up to $\mathcal{O}(1/m_W^4)$ in the amplitudes. To achieve this we expand the $W$-boson propagator in power series of $(q_j^2/m_W^2)$ as

$$-i\left[\frac{g^{\alpha\beta} - \frac{q_j^\alpha q_j^\beta}{m_W^2}}{q_j^2 - m_W^2}\right] \approx \frac{i}{m_W^2}\left[g^{\alpha\beta} + \frac{q_j^2}{m_W^2}\left(g^{\alpha\beta} - \frac{q_j^\alpha q_j^\beta}{q_j^2}\right)\right]. \tag{6}$$

The total amplitude can be expressed as $\mathcal{M} = \mathcal{M}_1 + \mathcal{M}_2 + \mathcal{M}_3$ and we calculate the differential cross section keeping all the amplitudes up to $\mathcal{O}(1/m_W^4)$. Since the neutrinos $\nu_\mu$ and $\bar{\nu}_e$ cannot be observed, we integrate the $\nu_\mu$ and $\bar{\nu}_e$ momenta, and define the $\nu_\mu\bar{\nu}_e$ invariant momentum as $q$. As the decay now looks like a three-body decay, it is meaningful to define effective Mandelstam-like variables constructed from the invariant momentum squared of the $e^-\nu_\mu\bar{\nu}_e$ system, denoted as $t$, and that of the $\gamma\nu_\mu\bar{\nu}_e$ system, denoted as $u$. Hence, $(p_e + q)^2 = t$ and $(p_\gamma + q)^2 = u$. Notice that $q^2$ is not a constant for our decay. It is, however, much more convenient to define the normalized parameters

$$x_p = \frac{t+u}{2(q^2 + m_\mu^2)},\quad y_p = \frac{t-u}{2(q^2 + m_\mu^2)},\quad q_p^2 = \frac{q^2}{(q^2 + m_\mu^2)}, \tag{7}$$

which can be written in terms of the observable quantities–the photon energy $E_\gamma$, the electron energy $E_e$, and the angle between the electron and photon $\theta$—as follows:

$$x_p = \frac{m_\mu(m_\mu - E_e - E_\gamma)}{2[m_\mu^2 - E_\gamma m_\mu - E_e m_\mu + E_e E_\gamma(1 - \cos\theta)]}, \tag{8}$$

$$y_p = \frac{m_\mu(E_e - E_\gamma)}{2[m_\mu^2 - E_\gamma m_\mu - E_e m_\mu + E_e E_\gamma(1 - \cos\theta)]}, \tag{9}$$

$$q_p^2 = \frac{m_\mu^2 - 2E_\gamma m_\mu - 2E_e m_\mu + 2E_e E_\gamma(1 - \cos\theta)}{2[m_\mu^2 - E_\gamma m_\mu - E_e m_\mu + E_e E_\gamma(1 - \cos\theta)]}. \tag{10}$$

The parameters of interest for the derivation $x_p$, $y_p$, and $q_p^2$ can easily be inverted in terms of the observables $E_e$, $E_\gamma$, and $\cos\theta$ as

$$E_e = \frac{m_\mu}{2}\left(\frac{1 - q_p^2 - x_p + y_p}{1 - q_p^2}\right), \tag{11}$$

$$E_\gamma = \frac{m_\mu}{2}\left(\frac{1 - q_p^2 - x_p - y_p}{1 - q_p^2}\right), \tag{12}$$

$$\cos\theta = \frac{(q_p^2 - x_p)^2 + 2x_p - y_p^2 - 1}{(1 - q_p^2 - x_p)^2 - y_p^2}. \tag{13}$$

We notice that replacing $y_p$ by $-y_p$ while keeping $q_p^2$ and $x_p$ unchanged actually results in swapping the energies of the photon and electron while keeping the angle between them unaltered. This feature will play a very crucial role in defining the observable asymmetry in Sec. III.

We have ignored the electron mass $m_e$ starting from Eq. (7) as it results in a significant simplification of the analytic expressions. It is of course well known that neglecting the electron mass results in the persistence of a wrong-helicity right-handed electron [18,19] in this decay as a result of inner bremsstrahlung from the electron (see second diagram of Fig. 1). The results are in obvious disagreement depending on whether $m_e$ is retained. We will therefore very carefully consider the issue of electron mass to justify the neglect of $m_e$ for our limited purpose of extracting $\eta_\gamma$, while acknowledging that $m_e$ should not be ignored in general. In order to retain maximum sensitivity to $\eta_\gamma$ the kinematic domain is chosen to minimize the soft photon and collinear singularity contributions; the effect of $m_e$ is found to be insignificant in the kinematic domain sensitive to $\eta_\gamma$. Our calculations have been verified while retaining $m_e$ throughout. Critical expressions including $m_e$ contributions are presented in the Appendix for clarity. Expressions for $x_p$ and $y_p$ are modified to accommodate the effects of $m_e$, while retaining an *apparent exchange symmetry* between $E_\gamma$ and $E_e$ under the newly defined variables $x_n$ and $y_n$ in Eq. (A6).

We consider only the normalized differential decay rate $\bar{\Gamma}(x_p, y_p, q_p^2)$ obtained after integrating the $\nu_\mu$ and $\bar{\nu}_e$ momenta, which is defined as

$$\bar{\Gamma}(x_p, y_p, q_p^2) = \frac{1}{\Gamma_\mu} \cdot \frac{d^3\Gamma}{dq_p^2 dx_p dy_p}, \tag{14}$$

where $\Gamma_\mu$ is the total decay width of the muon. In terms of these new normalized variables, the phase space for this process is bounded by three surfaces: $q_p^2 = 0$, $x_p = 1/2$, and $(q_p^4 - q_p^2 + x_p^2 - y_p^2) = 0$. It is easily seen from Eq. (13) that the plane $x_p = 1/2$ corresponds to $\theta = 0°$ and the curved surface $(q_p^4 - q_p^2 + x_p^2 - y_p^2) = 0$ signifies $\theta = 180°$. The physical region in $q_p^2$, $x_p$, and $y_p$ parameter space is given by

$$\begin{aligned} q_p\sqrt{1 - q_p^2} \le x_p \le \frac{1}{2}, \\ |y_p| \le \left(\frac{1}{2} - q_p^2\right), \\ (q_p^4 - q_p^2 + x_p^2 - y_p^2) \ge 0, \\ 0 \le q_p^2 \le \frac{1}{2}. \end{aligned} \tag{15}$$

Form Eqs. (7) and (15) it is clear that both $q_p^2$ and $x_p$ are positive-valued functions, whereas $y_p$ can have a positive value or a negative value and the physical region allows $y_p$ to have a range symmetric about $y_p = 0$. So, if $(x_p, y_p, q_p^2)$ is a point inside the physical region, $(x_p, -y_p, q_p^2)$ will also lie inside the allowed region. This motivates us to investigate the properties of the odd and even parts of $\bar{\Gamma}(x_p, y_p, q_p^2)$ under the variable $y_p$. In the next section (Sec. III) we construct such an observable as the ratio of the odd part in $y_p$ divided by the even part in $y_p$ of $\bar{\Gamma}(x_p, y_p, q_p^2)$ and demonstrate its heightened sensitivity to $\eta_\gamma$.

## III. OBSERVABLE AND ASYMMETRY

The "odd" and "even" parts $\bar{\Gamma}_o(x_p, y_p, q_p^2)$ and $\bar{\Gamma}_e(x_p, y_p, q_p^2)$, respectively, of the normalized differential decay rate (14) with respect to $y_p$ are defined as

$$\begin{aligned} \bar{\Gamma}_o(x_p, y_p, q_p^2) &= \frac{1}{2}[\bar{\Gamma}(x_p, y_p, q_p^2) - \bar{\Gamma}(x_p, -y_p, q_p^2)] \\ &\approx F_o(x_p, y_p, q_p^2) + \eta_\gamma G_o(x_p, y_p, q_p^2), \end{aligned} \tag{16}$$

$$\begin{aligned} \bar{\Gamma}_e(x_p, y_p, q_p^2) &= \frac{1}{2}[\bar{\Gamma}(x_p, y_p, q_p^2) + \bar{\Gamma}(x_p, -y_p, q_p^2)] \\ &\approx F_e(x_p, y_p, q_p^2) + \eta_\gamma G_e(x_p, y_p, q_p^2), \end{aligned} \tag{17}$$

where the small $\eta_\gamma^2$ terms are ignored.

As we have obtained $\bar{\Gamma}(x_p, y_p, q_p^2)$ by integrating a positive-valued function $|\mathcal{M}|^2$, it is obvious that both $\bar{\Gamma}(x_p, y_p, q_p^2)$ and $\bar{\Gamma}(x_p, -y_p, q_p^2)$ will be positive. Hence, $\bar{\Gamma}_e(x_p, y_p, q_p^2)$ [which is proportional to the sum of $\bar{\Gamma}(x_p, y_p, q_p^2)$ and $\bar{\Gamma}(x_p, -y_p, q_p^2)$] as well as $F_e(x_p, y_p, q_p^2)$ [which is the $\eta_\gamma \to 0$ limit of $\bar{\Gamma}_e(x_p, y_p, q_p^2)$] will always be greater than or equal to zero inside the physical region. On the other hand, $\bar{\Gamma}_o(x_p, y_p, q_p^2)$ [which is proportional to the difference between two positive quantities] as well as $F_o(x_p, y_p, q_p^2)$ [which is the $\eta_\gamma \to 0$ limit of $\bar{\Gamma}_o(x_p, y_p, q_p^2)$] could be positive, zero, or negative inside the allowed region.

We now define an observable $R_\eta$ as

$$R_\eta(x_p, y_p, q_p^2) = \frac{\bar{\Gamma}_o}{\bar{\Gamma}_e} \approx \frac{F_o}{F_e}\left[1 + \eta_\gamma\left(\frac{G_o}{F_o} - \frac{G_e}{F_e}\right)\right] \tag{18}$$

and the asymmetry $A_\eta(x_p, y_p, q_p^2)$ in $R_\eta$ as

$$A_\eta(x_p, y_p, q_p^2) = \left(\frac{R_\eta}{R_{\rm SM}} - 1\right) \approx \eta_\gamma\left(\frac{G_o}{F_o} - \frac{G_e}{F_e}\right), \tag{19}$$

where

$$R_{\rm SM} = \frac{\bar{\Gamma}_o}{\bar{\Gamma}_e}\bigg|_{\eta_\gamma = 0} = \frac{F_o}{F_e}.$$

Since, $F_o$ and $G_o$ are the zeroth-order and first-order terms, respectively, in the expansion of the odd part of $\bar{\Gamma}(x_p, y_p, q_p^2)$ with respect to $\eta_\gamma$ [see Eq. (16)], both of them are expected to be proportional to odd powers of $y_p$, rendering the ratio $(G_o/F_o)$ finite at $y_p = 0$.

We will now show that $F_o$, i.e., the odd part of the SM, has a zero for this mode for all $q_p^2$. For simplicity, to describe the situation mathematically we consider only the dominant contributions arising from the first and second Feynman diagrams in Fig. 1. Retaining only relevant terms up to $\mathcal{O}(1/m_W^4)$, we can write

$$F_o \propto y_p h(x_p, y_p, q_p^2) f(x_p, y_p, q_p^2), \tag{20}$$

where

$$h = \left[\frac{1+q_p^2}{(1-q_p^2)^5(1-2x_p)\{(1-q_p^2-x_p)^2-y_p^2\}^2}\right], \tag{21}$$

$$\begin{aligned} f = [&7q_p^8 - 4(4-x_p)q_p^6 + (11-4x_p+6x_p^2-6y_p^2)q_p^4 \\ &- 2q_p^2(1-x_p+8x_p^2-6x_p^3-4y_p^2+2x_py_p^2) \\ &+ 3x_p^4 - 12x_p^3 + x_p^2(11-2y_p^2) - x_p(2-4y_p^2) \\ &- y_p^2(3+y_p^2)]. \end{aligned} \tag{22}$$

As can be seen from the inequalities in Eq. (15), $h(x_p, y_p, q_p^2)$ is always positive inside the physical region. Hence, the deciding factor for the sign of $F_o$ is only $f(x_p, y_p, q_p^2)$. Now, on the $x_p = 1/2$ surface we have

$$f\left(\frac{1}{2}, y_p, q_p^2\right) = \frac{7}{16}(1-2q_p^2)^4 - \frac{3}{2}(1-2q_p^2)^2 y_p^2 - y_p^4,$$

which after using the upper limit of $|y_p|$ from Eq. (15) implies that

$$f\left(\frac{1}{2}, y_p, q_p^2\right) \geq 0, \tag{23}$$

$$\Rightarrow F_o\left(\frac{1}{2}, |y_p|, q_p^2\right) \geq 0, \tag{24}$$

$$F_o\left(\frac{1}{2}, -|y_p|, q_p^2\right) \leq 0. \tag{25}$$

Similarly, for any point on the curved surface $(q_p^4 - q_p^2 + x_p^2 - y_p^2) = 0$ denoted as $C$, we have $y_p^2 = (q_p^4 - q_p^2 + x_p^2)$ and hence

$$f(x_p, y_p, q_p^2)|_C = (1-q_p^2)(1-2x_p)^2(q_p^2 - 2x_p). \tag{26}$$

Upon using the limits of $x_p$ and $q_p^2$ from Eq. (15), it can be easily shown that

$$f(x_p, y_p, q_p^2)|_C \leq 0, \tag{27}$$

$$\Rightarrow F_o(x_p, |y_p|, q_p^2)|_C \leq 0, \tag{28}$$

$$F_o(x_p, -|y_p|, q_p^2)|_C \geq 0. \tag{29}$$

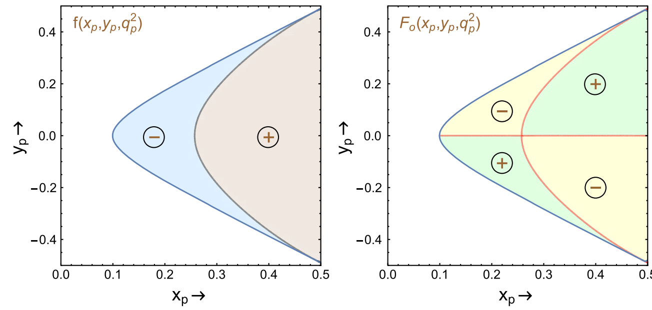


FIG. 3. The variations of the functions $f(x_p, y_p, q_p^2)$ and $F_o(x_p, y_p, q_p^2)$ are shown in the $x_p$-$y_p$ plane in the left and right panels, respectively, where $q_p^2 = 0.01$. The blue line in both panels indicates one boundary of the phase space with $\cos\theta = -1$ or $(q_p^4 - q_p^2 + x_p^2 - y_p^2) = 0$. In the left panel, the blue region indicates a negative-valued $f(x_p, y_p, q_p^2)$, the brown region indicates a positive-valued $f(x_p, y_p, q_p^2)$, and the black curve indicates $f(x_p, y_p, q_p^2) = 0$. In the right panel, the yellow region indicates a negative-valued $F_o(x_p, y_p, q_p^2)$, the green region indicates a positive-valued $F_o(x_p, y_p, q_p^2)$, and the red curve indicates $F_o(x_p, y_p, q_p^2) = 0$.

We have concluded that $f(x_p, y_p, q_p^2) < 0$ along the curve $C$ and $f(x_p, y_p, q_p^2) > 0$ at the other boundary surface $x_p = 1/2$. It is therefore obvious that there must be at least one surface within the allowed phase space region where $f(x_p, y_p, q_p^2) = 0$. In the first plot of Fig. 3, the blue region indicates $f(x_p, y_p, q_p^2) < 0$ and the brown region indicates $f(x_p, y_p, q_p^2) > 0$, whereas the black curve indicates $f(x_p, y_p, q_p^2) = 0$. In the second plot of Fig. 3, the yellow region indicates $F_o(x_p, y_p, q_p^2) < 0$ and the green region indicates $F_o(x_p, y_p, q_p^2) > 0$, while the red curve indicates $F_o(x_p, y_p, q_p^2) = 0$.

The odd ($\bar{\Gamma}_o$) and even ($\bar{\Gamma}_e$) parts of the differential rate as well as the four functions $F_o$, $F_e$, $G_o$, and $G_e$ contain soft collinear divergences arising due to $E_\gamma = 0$ or $\cos\theta = 1$ and a divergence due to the vanishing $E_e$ if $m_e$ is ignored. It is obvious form Eq. (12) that soft photons dominate in the region corresponding to $(x_p + y_p) \approx (1 - q_p^2)$, which implies that $(x_p + y_p)$ is close to its maximum value. Hence, events with small photon energies lie in the top corner of Fig. 3 where the blue curve meets the $x_p = ½$ line. Similarly, one can see from Eq. (11) that small electron energies implies $(x_p - y_p) \approx (1 - q_p^2)$, and these events lie in the bottom corner of Fig. 3 where the blue curve meets the $x_p = ½$ line. For any value of $q_p^2$, the collinear divergence occurs along the $x_p = ½$ line as can easily be seen from Eq. (13). These singularities are evident from Eq. (21) and occur in each of $\bar{\Gamma}$, $\bar{\Gamma}_o$, and $\bar{\Gamma}_e$ as well as the four functions $F_o$, $F_e$, $G_o$, and $G_e$. It is only in these regions that an expansion in powers of $m_e/m_\mu$ is not valid: the electron mass needs to be retained, and ignoring it alters the differential decay rates. To deal with the $x_p = ½$ collinear singularity we choose an appropriate cut on $x_p$ which is also necessitated by experimental resolution. It can be seen from Eq. (19), however, that within the SM $A_\eta$ is finite and zero, even in the regions plagued by collinear soft photon singularities and the ones that arise due to the neglect of $m_e$. Note that in $A_\eta$ the $h$ function in Eq. (21) carrying the singular denominator cancels. The zero observed in $F_o$ and the consequent singularity in the asymmetry $A_\eta$ has nothing to do with the well-known collinear soft photon and $m_e \to 0$ singularities. The zero observed in $F_o$ is genuine and looks like an apparent exchange symmetry between $E_e$ and $E_\gamma$ only for appropriately chosen parameters $x_p$ and $y_p$ [or $x_n$ and $y_n$ defined in Eq. (A6)] with $m_e$ retained.

We have explicitly demonstrated that there exists a surface (besides the $y_p = 0$ plane) where $F_o(x_p, y_p, q_p^2) = 0$; we refer to this surface corresponding to the *"new type of zero"* as the "null surface." This means that at each point on this surface the differential decay rate $\bar{\Gamma}(x_p, y_p, q_p^2)$ remains unaltered if we interchange the energies of the photon and electron. Hence, $A_\eta(x_p, y_p, q_p^2)$ diverges on the null surface for any nonzero value of $\eta_\gamma$ and becomes zero everywhere in the phase space when $\eta_\gamma$ is zero. The null surface divides the phase space into two regions: one where $A_\eta$ is positive and one where $A_\eta$ is negative. For $\eta_\gamma > 0$, $A_\eta < 0$ for $x_p$ values smaller than the values indicated by the null surface, whereas $A_\eta > 0$ for $x_p$ values larger than the values indicated by the null surface. However, if $\eta_\gamma < 0$ the opposite behavior in the signs of $A_\eta$ is seen. This feature can be used to determine the sign of $\eta_\gamma$. To measure the value of $\eta_\gamma$ experimentally, one must average $A_\eta$ over specified regions of phase space where it could be positive or negative. Such averages are necessitated by the experimental resolutions for $q_p^2$, $x_p$, and $y_p$ and will in general reduce the asymmetry. Hence, it is convenient to use $|A_\eta|$ as the asymmetry.

In the next section (Sec. IV) we probe the feasibility of measuring $\eta_\gamma$ using the asymmetry obtained in this section.

## IV. SIMULATION AND ANALYSIS

In order to study the sensitivity of the muon radiative decay mode we need to include the resolutions of the photon energy, electron energy, and the angle between them. We take them to be 2%, 0.5%, and 10 mrad, respectively [20]. As can be seen from Eqs. (11)–(13), the resolutions for $x_p$, $y_p$, and $q_p^2$ will also vary at different points in phase space due to the functional forms of these parameters. We begin by evaluating the resolutions for $x_p$, $y_p$, and $q_p^2$ for the entire allowed phase space. We find that the resolutions for $x_p$, $y_p$, and $q_p^2$ are always less than 0.01, 0.02, and 0.02, respectively. For simplicity, in our simulation we take the worst possible scenario and assume constant resolutions for $x_p$, $y_p$, and $q_p^2$ corresponding to their largest values of 0.01, 0.02, and 0.02, respectively, throughout the entire allowed phase space, which allows us to choose equal-size bins. Hence, the phase space region $0 \le q_p^2 \le ½$, $0 \le x_p \le ½$, $-½ \le y_p \le ½$ is divided into 25 bins in $q_p^2$ and 50 bins in both $x_p$ and $y_p$, all of equal size. Among these bins, only 6378 bins lie inside the physical phase space region. We next estimate the systematic and statistical errors for $|A_\eta|$ in each of these bins, assuming $\eta_\gamma = 0.01$.

To find the systematic error in $|A_\eta|$ for the $i$th bin, we evaluate it at 62 500 equally spaced points in that bin to estimate $|A_\eta|_i^j$, where $j$ is the index of a point inside the $i$th bin. However, for the bins near the boundary of the phase space, all of these points will not be inside the physical region and hence we denote the number of physical points inside the $i$th bin as $n_i$. We now calculate the average of $|A_\eta|_i^j$ inside a bin, i.e.,

$$\langle |A_\eta|_i \rangle = \frac{1}{n_i} \sum_j |A_\eta|_i^j,$$

and take this as the asymmetry of that bin. Then we take the systematic error as the average deviation of $|A_\eta|_i^j$, i.e.,

$$\sigma_i^{\rm sys} = \frac{1}{n_i} \sum_j |\langle |A_\eta|_i \rangle - |A_\eta|_i^j|.$$

Ideally, the errors can and should have been calculated using a standard Monte Carlo technique with a larger number of sample points. The approach followed in this paper is to express the integral as a Riemann sum only for simplicity.

The statistical error for $|A_\eta|$ in each bin is also estimated by averaging it at the same 62 500 equally spaced points. Note that while $A_\eta$ is divergent on the null surface, the average value of $|A_\eta|$ for the $i$th bin, i.e., $\langle |A_\eta|_i \rangle$ estimated from Monte Carlo studies is never larger than $10^{-6}$ for any bin. Hence,

$$\sigma_i^{\rm sta} = \sqrt{\frac{1 - \langle |A_\eta|_i \rangle^2}{N_i}} \approx \frac{1}{\sqrt{(N_{\rm SM})_i}},$$

where $i$ is the index of the bins and $N_i$ represents the number of events inside the $i$th bin, which is almost the same as $(N_{\rm SM})_i$, the number of SM events for the $i$th bin. We have also assumed that both $A_\eta$ and the effects of $\eta_\gamma$ on $N_i$ are small and can be ignored. If this were not the case, $N_i$ would itself be sensitive to $\eta_\gamma$, contrary to our simulation results. Hence, we simply take the statistical error for all practical purposes to be the same as that in SM events. The number of events in each bin is calculated by taking the total number of muons to be $10^{19}$. To avoid the singularities

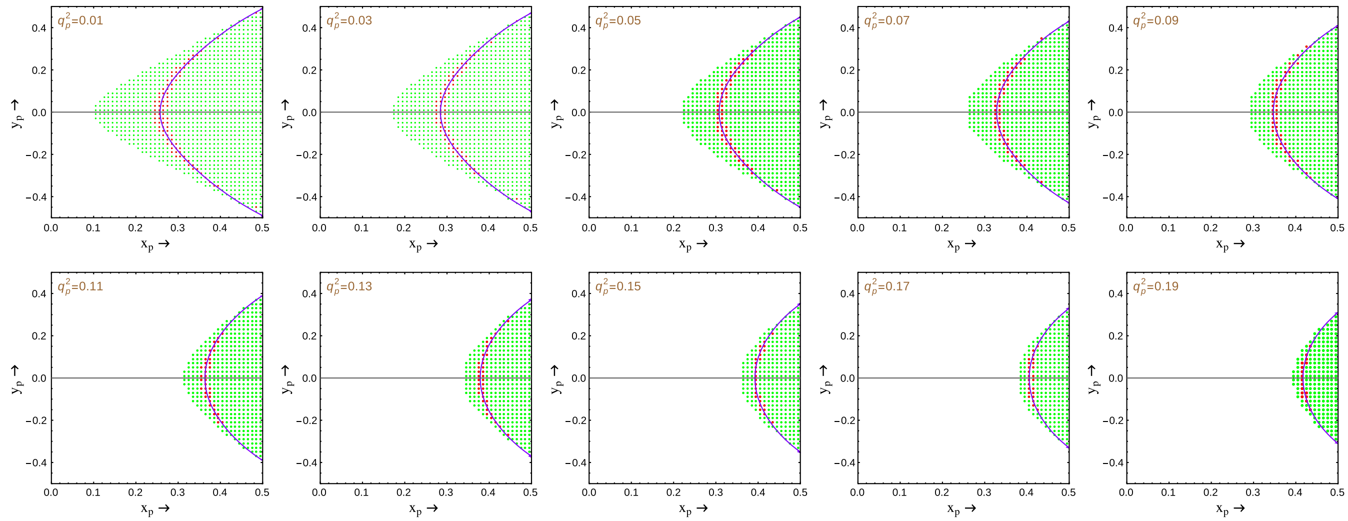


FIG. 4. The variation of $F_o(x_p, y_p, q_p^2)$ for different $q_p^2$ in the $x_p$-$y_p$ plane. Each green dot represents a bin according to the experimental resolutions of the photon energy, electron energy, and the angle between them. The red dots stand for the bins with $\delta|A_\eta|/|A_\eta| \le 10$ in that bin. The purple curve indicates $F_o = 0$ in a different $q_p^2$ plane. Our numerical analysis includes the bins corresponding to the red dots only. This results in an optimal sensitivity to $\eta_\gamma$.

in the number of SM events for the bins near the $x_p = ½$ plane, we ignore the bins with $0.49 \le x_p \le 0.5$.

The total error in $|A_\eta|$ for any particular bin is then given by $\delta|A_\eta|_i = \sqrt{(\sigma_i^{\rm sta})^2 + (\sigma_i^{\rm sys})^2}$. This error in $|A_\eta|$ will affect the measurement of $\eta_\gamma$. Using Eq. (19), the error in the measurement of $\eta_\gamma$ in each bin is

$$\left|\frac{\delta\eta_\gamma}{\eta_\gamma}\right|_i = \frac{\delta|A_\eta|_i}{|A_\eta|_i}, \tag{30}$$

where $|A_\eta|_i \equiv \langle|A_\eta|_i\rangle$ and we take the theoretical function $(G_o/F_o - G_e/F_e)$ to be free from experimental uncertainties. It is obvious from Eq. (30) that the highest sensitivity is achieved in bins close to the null surface where $|A_\eta|_i$ is the largest. Hence, we consider only the region along the null surface by applying a cut $\delta|A_\eta|_i/|A_\eta|_i \le 10$ to determine $\eta_\gamma$.

In Fig. 4 we indicate the bins that satisfy the above cut by red dots for different $q_p^2$ values, whereas the green dots indicate all of the other bins inside the physical region; the purple curve indicates the null surface where $F_o = 0$ for the corresponding $q_p^2$ value. Including only the bins that satisfy the above cut for a simulated value of $\eta_\gamma = 0.01$ (at one loop in the SM, $|\eta_\gamma| \lesssim 0.015$), we estimate an error of $\delta\eta_\gamma = 2.6 \times 10^{-3}$, implying a $3.9\sigma$ significance for the measurement. With a long-term goal of producing $10^{19}$ muons, the next round of experiments aim to produce $10^{18}$ muons/year. This reduces the sensitivity from $3.9\sigma$ to $1.4\sigma$. To appreciate the advantage of radiative muon decays in measuring the $WW\gamma$ vertex, one needs to note that the current global average of $\kappa_\gamma$ differs from unity by only $0.4\sigma$. We note that the significance of the measured value of $\eta_\gamma$ may in principle be improved by optimizing the chosen cut and binning procedure. However, we refrain from such intricacies as our approach is merely to present a proof of principle.

We have shown that the sensitivity to $\eta_\gamma$ arises due to the vanishing of the odd differential decay rate in the standard model, denoted by $F_o$. The observed singularity in $A_\eta$ is unrelated to the soft photon and collinear singularities or the singularity arising due to neglecting $m_e$ in calculations. The most sensitive region to measure $\eta_\gamma$ is where $A_\eta$ is large and obviously lies along the zero of $F_o$, as indicated by Eq. (19). The region around $F_o = 0$, for which $\delta|A_\eta|_i/|A_\eta|_i \le 10$, is where a legitimate expansion in powers of $m_e/m_\mu$ can be carried out and is distinct from the singular regions in the differential decay rates where such an expansion cannot be done. However, in order to verify the accuracy of the sensitivity achievable in $\eta_\gamma$ measurements the calculations have been redone by numerically retaining $m_e$. We found that for the bins represented by red dots in Fig. 4 the maximum correction in $\eta_\gamma$ is $\mathcal{O}(10^{-4})$, which is an order of magnitude smaller than its error, $\delta\eta_\gamma = 2.6 \times 10^{-3}$.

Finally, we discuss possible sources of inaccuracies in our estimation of the uncertainty. Higher-order electroweak corrections to the process considered will modify the decay rate and alter $F_o$. While higher-order electroweak corrections have not been included in our analysis, they have been worked out in detail [21]. However, this is unlikely to affect our analysis technique as we have selected bins to be included in estimating $\eta_\gamma$ based purely on the criterion $\delta|A_\eta|_i/|A_\eta|_i \le 10$ and not on the location and validity of the null surface. A possible source of uncertainty that we have ignored in our analysis is the assumption that the muon decays at rest or with known four-momenta. While facilities that produce large numbers of muons are designed to bring the muons to rest, a fraction of them may decay with a finite but unknown four-momenta, rendering the exact measurement of $q_p^2$ inaccurate. This effect can in principle be considered by including additional systematic errors in $q_p^2$.

## V. CONCLUSION

In order to probe the lepton-flavor-violating process $\mu \to e\gamma$ facilities that produce large numbers of muons are being designed. We have shown that radiative muon decay $\mu \to e\gamma\nu_\mu\bar{\nu}_e$ is a promising mode to probe loop-level corrections in the SM to the $C$- and $P$-conserving dimension-four $WW\gamma$ vertex with good accuracy. The process has two missing neutrinos in the final state, and upon integrating their momenta the partial differential decay rate removes the well-known radiation-amplitude zero. However, we have shown that the normalized differential decay rate, which is odd under the exchange of photon and electron energies, does have a zero in the case of the SM. This *new type of zero* has hitherto not been studied in the literature. A suitably constructed asymmetry using this fact enables a sensitive probe for the $WW\gamma$ vertex beyond the SM. The large number of muons produced keeps the statistical error in control for a tiny part of the physical phase space, enabling us to measure $\eta_\gamma = 0.01$ with $3.9\sigma$ significance.

## ACKNOWLEDGMENTS

We thank Yoshitaka Kuno, Marcin Chrząszcz, Thomas G. Rizzo, and Jernej F. Kamenik for valuable suggestions and discussions. The work of R. M. is supported in part by Grants No. FPA2014-53631-C2-1-P, No. FPA2017-84445-P, and No. SEV-2014-0398 (AEI/ERDF, EU) and by PROMETEO/2017/053.

## APPENDIX: EXPRESSIONS WITH ELECTRON MASS RETAINED

In the presence of the electron mass $m_e$, we have $s + t + u = q^2 + m_\mu^2 + m_e^2$, where the Mandelstam variables are defined as $(p_e + p_\gamma)^2 = s$, $(p_e + q)^2 = t$, and $(p_\gamma + q)^2 = u$. The physical region is determined by the following inequalities [22]:

$$m_e^2 \le s \le \left(m_\mu - \sqrt{q^2}\right)^2, \tag{A1}$$

$$q^2 \le u \le (m_\mu - m_e)^2, \tag{A2}$$

$$\left(m_e + \sqrt{q^2}\right)^2 \le t \le m_\mu^2, \tag{A3}$$

$$G[s, u, m_\mu^2, 0, m_e^2, q^2] \le 0, \tag{A4}$$

where

$$G[x, y, z, u, v, w] = -\frac{1}{2}\begin{vmatrix} 0 & 1 & 1 & 1 & 1 \\ 1 & 0 & v & x & z \\ 1 & v & 0 & u & y \\ 1 & x & u & 0 & w \\ 1 & z & y & w & 0 \end{vmatrix}. \tag{A5}$$

We define the variables $x_n$, $y_n$, and $q_n^2$, which reduce to $x_p$, $y_p$, and $q_p^2$ in the $m_e \to 0$ limit, in the following way:

$$x_n = \frac{t + u}{2(q^2 + m_\mu^2 + m_e^2)},$$
$$y_n = \frac{t - u + m_e^2}{2(q^2 + m_\mu^2 + m_e^2)},$$
$$q_n^2 = \frac{q^2}{(q^2 + m_\mu^2 + m_e^2)}. \tag{A6}$$

The energies of the electron and photon are obtained from the above definitions as

$$E_e = \frac{(2m_\mu^2 + m_e^2)(1 - q_n^2 - x_n + y_n) - m_e^2(x_n - y_n)}{4m_\mu(1 - q_n^2)}, \tag{A7}$$

$$E_\gamma = \frac{(2m_\mu^2 + m_e^2)(1 - q_n^2 - x_n - y_n) - m_e^2(x_n + y_n)}{4m_\mu(1 - q_n^2)}. \tag{A8}$$

Under the replacement $y_n \to -y_n$, the electron and photon energies get exchanged and one can separate the odd and even parts of the differential decay rate as follows:

$$\bar{\Gamma}_o(x_n, y_n, q_n^2) = \frac{1}{2}[\bar{\Gamma}(x_n, y_n, q_n^2) - \bar{\Gamma}(x_n, -y_n, q_n^2)],$$
$$\bar{\Gamma}_e(x_n, y_n, q_n^2) = \frac{1}{2}[\bar{\Gamma}(x_n, y_n, q_n^2) + \bar{\Gamma}(x_n, -y_n, q_n^2)]. \tag{A9}$$

The $h$ function in Eq. (21) containing a singular denominator now becomes

$$h \propto \frac{1}{E_e^2 E_\gamma^2 (m_\mu^2(1 - 2x_n) + m_e^2(q_n^2 - 2x_n))}. \tag{A10}$$

In the region around $F_o = 0$ (denoted by red dots in Fig. 4), a legitimate expansion in powers of $(m_e/m_\mu)$ for the expressions of $\bar{\Gamma}_o$ and $\bar{\Gamma}_e$ can be carried out in the following way:

$$\bar{\Gamma}_o \approx (F_o + (m_e/m_\mu)^2 \delta F_o) + \eta_\gamma (G_o + (m_e/m_\mu)^2 \delta G_o), \tag{A11}$$

$$\bar{\Gamma}_e \approx (F_e + (m_e/m_\mu)^2 \delta F_e) + \eta_\gamma (G_e + (m_e/m_\mu)^2 \delta G_e), \tag{A12}$$

where the small $\eta_\gamma^2$ terms are ignored. Here, $\delta F_o$, $\delta G_o$, $\delta F_e$, and $\delta G_e$ are the leading-order correction terms due to the nonzero electron mass. The observable $R_\eta$ is modified as

$$\begin{aligned} R_\eta(x_n, y_n, q_n^2) &= \frac{\bar{\Gamma}_o(x_n, y_n, q_n^2)}{\bar{\Gamma}_e(x_n, y_n, q_n^2)} \\ &\approx \left( \frac{F_o + (\frac{m_e}{m_\mu})^2 \delta F_o}{F_e + (\frac{m_e}{m_\mu})^2 \delta F_e} \right) \left[ 1 + \eta_\gamma \left( \frac{G_o + (\frac{m_e}{m_\mu})^2 \delta G_o}{F_o + (\frac{m_e}{m_\mu})^2 \delta F_o} - \frac{G_e + (\frac{m_e}{m_\mu})^2 \delta G_e}{F_e + (\frac{m_e}{m_\mu})^2 \delta F_e} \right) \right]. \end{aligned} \tag{A13}$$

Hence, the asymmetry $A_\eta(x_p, y_p, q_p^2)$ in $R_\eta$ becomes

$$\begin{aligned} A_\eta(x_n, y_n, q_n^2) &= \left( \frac{R_\eta}{R_{\mathrm{SM}}} - 1 \right) \\ &\approx \eta_\gamma \left( \frac{G_o + (\frac{m_e}{m_\mu})^2 \delta G_o}{F_o + (\frac{m_e}{m_\mu})^2 \delta F_o} - \frac{G_e + (\frac{m_e}{m_\mu})^2 \delta G_e}{F_e + (\frac{m_e}{m_\mu})^2 \delta F_e} \right) \\ &\approx \eta_\gamma \left( \frac{G_o}{F_o} - \frac{G_e}{F_e} \right) + \eta_\gamma \left( \frac{m_e}{m_\mu} \right)^2 \left( \frac{G_e \delta F_e}{F_e^2} - \frac{G_o \delta F_o}{F_o^2} + \frac{\delta G_o}{F_o} - \frac{\delta G_e}{F_e} \right), \end{aligned} \tag{A14}$$

where

$$R_{\mathrm{SM}} = \frac{\bar{\Gamma}_o}{\bar{\Gamma}_e}\bigg|_{\eta_\gamma = 0} = \left( \frac{F_o + (\frac{m_e}{m_\mu})^2 \delta F_o}{F_e + (\frac{m_e}{m_\mu})^2 \delta F_e} \right).$$

Note that the above expansion in $\mathcal{O}(m_e/m_\mu)$ fails in the region where collinear or soft photon divergences occur.


[1] S. Chatrchyan *et al.* (CMS Collaboration), Phys. Rev. D **89**, 092005 (2014).
[2] G. Aad *et al.* (ATLAS Collaboration), Phys. Rev. D **87**, 112003 (2013).
[3] V. M. Abazov *et al.* (D0 Collaboration), Phys. Lett. B **718**, 451 (2012).
[4] T. Aaltonen *et al.* (CDF Collaboration), Phys. Rev. Lett. **104**, 201801 (2010).
[5] J. Abdallah *et al.* (DELPHI Collaboration), Eur. Phys. J. C **66**, 35 (2010).
[6] S. Schael *et al.* (ALEPH Collaboration), Phys. Lett. B **614**, 7 (2005).
[7] G. Abbiendi *et al.* (PAL Collaboration), Eur. Phys. J. C **33**, 463 (2004).
[8] P. Achard *et al.* (L3 Collaboration), Phys. Lett. B **586**, 151 (2004).
[9] G. Couture and J. N. Ng, Z. Phys. C **35**, 65 (1987).
[10] C. Patrignani *et al.* (Particle Data Group), Chin. Phys. C **40**, 100001 (2016).
[11] K. O. Mikaelian, M. A. Samuel, and D. Sahdev, Phys. Rev. Lett. **43**, 746 (1979).
[12] COMET Collaboration, http://comet.kek.jp/.
[13] MEG Collaboration, https://meg.web.psi.ch/.
[14] Mu2e Collaboration, http://mu2e.fnal.gov/public/hep/general/proposals.shtml.
[15] Y. Kuno and Y. Okada, Rev. Mod. Phys. **73**, 151 (2001).
[16] K. Hagiwara, R. D. Peccei, and D. Zeppenfeld, Nucl. Phys. **B282**, 253 (1987).
[17] W. J. Marciano and A. Queijeiro, Phys. Rev. D **33**, 3449 (1986).
[18] L. M. Sehgal, Phys. Lett. B **569**, 25 (2003).
[19] V. S. Schulz and L. M. Sehgal, Phys. Lett. B **594**, 153 (2004).
[20] Y. Kuno (private communication).
[21] A. B. Arbuzov and E. S. Scherbakova, Phys. Lett. B **597**, 285 (2004); M. Fael, L. Mercolli, and M. Passera, Phys. Rev. D **88**, 093011 (2013); J. High Energy Phys. 07 (2015) 153; G. M. Pruna, A. Signer, and Y. Ulrich, Phys. Lett. B **772**, 452 (2017).
[22] E. Byckling and K. Kajantie, *Particle Kinematics* (John Wiley & Sons, Bristol, 1972), pp. 106–107.